Size- and shape-dependent foreign body immune response to materials implanted in rodents and non-human primates

Omid Veiseh[1,2,3†], Joshua C. Doloff[1,3†], Minglin Ma[1,3,4†‡], Arturo J. Vegas[1,3], Hok Hei Tam[1,2], Andrew R. Bader[1,3], Jie Li[1,3], Erin Langan[1,3], Jeffrey Wyckoff[1], Whitney S. Loo[2], Siddharth Jhunjhunwala[1,3], Alan Chiu[1,3], Sean Siebert[1,3], Katherine Tang[1,3], Jennifer Hollister-Lock[4], Stephanie Aresta-Dasilva[1,3], Matthew Bochenek[5], Joshua Mendoza-Elias[5], Yong Wang[5], Merigeng Qi[5], Danya M. Lavin[1,3], Michael Chen[1,3], Nimit Dholakia[1,3], Raj Thakrar[1,3], Igor Lacík[6], Gordon C. Weir[4], Jose Oberholzer[5], Dale L. Greiner[7], Robert Langer[1,2,3,8,9,10] and Daniel G. Anderson[1,2,3,8,9,10]★

The efficacy of implanted biomedical devices is often compromised by host recognition and subsequent foreign body responses. Here, we demonstrate the role of the geometry of implanted materials on their biocompatibility *in vivo*. In rodent and non-human primate animal models, implanted spheres 1.5 mm and above in diameter across a broad spectrum of materials, including hydrogels, ceramics, metals and plastics, significantly abrogated foreign body reactions and fibrosis when compared with smaller spheres. We also show that for encapsulated rat pancreatic islet cells transplanted into streptozotocin-treated diabetic C57BL/6 mice, islets prepared in 1.5-mm alginate capsules were able to restore blood-glucose control for up to 180 days, a period more than five times longer than for transplanted grafts encapsulated within conventionally sized 0.5-mm alginate capsules. Our findings suggest that the *in vivo* biocompatibility of biomedical devices can be significantly improved simply by tuning their spherical dimensions.

Biomaterials and devices implanted in the body are used for a broad spectrum of clinical applications, including cell transplantation[1], controlled drug release[2], continuous sensing and monitoring of physiological conditions[3], electronic pacing[4] and tissue regeneration[5]. For many of these applications the performance of the device is dependent on its interaction with the host immune system[6]. Immune recognition initiates a cascade of cellular processes leading to foreign body reactions, which include persistent inflammation, formation of foreign body giant cells (fused macrophages), fibrosis (walling-off) and damage to the surrounding tissue[7,8]. Even when devices are prepared using non-reactive biomaterials, a 100-μm thick fibrotic tissue often builds up (<1 month), enveloping the implanted device[9]. These unwanted effects can be both deleterious to the function of the device and a cause of significant pain and discomfort for the patient[9,10].

In attempting to develop more biocompatible materials and devices, researchers have investigated a range of parameters, including tuning material physiochemical properties to limit protein fouling[11,12], applying cell-resistive coatings[13], modifying surfaces with ligands to selectively modulate immune cell recruitment[14,15], and controlling surface porosity[16]. However, only a limited number of studies have examined the role of material or device geometry on modulating foreign body responses and fibrosis[17-20]. In particular, researchers evaluated various medical-grade polymers, which were extruded into geometries of rods with circular-, triangular- and pentagonal-shaped cross-sections, and then implanted these materials into rat gluteal muscles for 14 days[19]. Among the shapes tested, circular rods produced the least amount of foreign body responses, followed by pentagonal and then triangular. Other researchers described that implant shape can profoundly affect macrophage behaviour at the interface of percutaneous implants, and observed that smooth, well-contoured implants with no acute angles are more biocompatible[20]. Since these notable studies it has long been accepted that indeed materials with smooth surfaces are likely to be more biocompatible than those with sharp edges[19]; however, there is still no consensus on an ideal geometry[21].

[1]David H Koch Institute for Integrative Cancer Research, Massachusetts Institute of Technology, 500 Main Street, Cambridge, Massachusetts 02139, USA. [2]Department of Chemical Engineering, Massachusetts Institute of Technology, 77 Massachusetts Avenue, Cambridge, Massachusetts 02139, USA. [3]Department of Anesthesiology, Boston Children's Hospital, 300 Longwood Ave, Boston, Massachusetts 02115, USA. [4]Section on Islet Cell and Regenerative Biology, Research Division, Joslin Diabetes Center, One Joslin Place, Boston, Massachusetts 02215, USA. [5]Division of Transplantation, Department of Surgery, University of Illinois at Chicago, 840 South Wood Street, Chicago, Illinois 60612, USA. [6]Department for Biomaterials Research, Polymer Institute of the Slovak Academy of Sciences, Dubravska cesta 9, 845 41 Bratislava, Slovakia. [7]Program in Molecular Medicine, University of Massachusetts Medical School, Worcester, Massachusetts 01605, USA. [8]Division of Health Science Technology, Massachusetts Institute of Technology, 77 Massachusetts Avenue, Cambridge, Massachusetts 02139, USA. [9]Institute for Medical Engineering and Science, Massachusetts Institute of Technology, 77 Massachusetts Avenue, Cambridge, Massachusetts 02139, USA. [10]Harvard-MIT Division of Health Science and Technology, Massachusetts Institute of Technology, 77 Massachusetts Avenue, Cambridge, Massachusetts 02139, USA. †These authors contributed equally to this work. ‡Present address: Biological and Environmental Engineering, Cornell University, Ithaca, New York 14853, USA. *e-mail: dgander@mit.edu

Surface porosity has also been identified as an influential parameter affecting angiogenesis[16,22]. For example, researchers evaluated the role of surface porosity in promoting angiogenesis by comparing polytetrafluoroethylene (PTFE) membranes with pore sizes of 5 µm against membranes with pore sizes of 0.02 µm (ref. 22). This study demonstrated that the larger pore membranes had 80–100 times as many vascular structures associated with the implant. More recently, researchers have studied a wider range of pore sizes (0–80 µm) and demonstrated that an even stronger angiogenic response could be produced by tuning the pore sizes specifically to 30–40 µm (ref. 16).

At the macro level (>100 µm in size), it is generally held that thicker materials produce a proportionally higher magnitude of foreign body responses and fibrosis[3,21]. Another study examined the influence of material size by comparing host responses to polyurethane substrates prepared as cylinders that were either 300 or 2,000 µm in diameter. It was found that increasing the size of implanted materials resulted in larger foreign body reactions and in the formation of a thicker layer of fibrosis around the implant[23]. Interestingly, to our knowledge no one has studied the effect of sphere diameter on biocompatibility.

In this study, we sought to examine the role of spherical biomaterial geometry on biocompatibility *in vivo*. Our initial work focused on interrogating immune responses and fibrosis on implantation of alginate hydrogels. Commonly prepared as microspheres of 100–1,000 µm in diameter, alginate hydrogels are widely used for a number of *in vivo* applications, including controlled drug release, tissue regeneration and immunoisolation of therapeutic cells[24,25]. One biomedical application for which alginate microspheres (0.3–1 mm in diameter) have been extensively evaluated is the immunoisolation of donor pancreatic islets for the treatment of Type-1 diabetes[1,26]. Host recognition and fibrosis of alginate capsules in humans, independent of donor tissue, is the key barrier to the clinical translation of encapsulated donor islets for the treatment of type-1 diabetes[26–28]. When implanted into the intraperitoneal space of non-human primates or immunocompetent rodents, alginate microspheres elicit foreign body reactions and fibrosis[29,30]. To ensure proper biocompatibility assessment in our studies, we used an immunocompetent C57BL/6 mouse model for our initial screening, because this strain is known to produce strong fibrotic and foreign body responses that are similar to those observed in human patients[31].

To investigate the effect of sphere diameter on biocompatibility, we fabricated Ba$^+$-crosslinked SLG20 alginate hydrogel spheres in eight different sizes, 0.3 mm, 0.4 mm, 0.5 mm, 0.7 mm, 0.9 mm, 1 mm, 1.5 and 1.9 mm, with very narrow size distributions (Supplementary Fig. 1). These spheres (350 µl/mouse) were then implanted into the intraperitoneal space of C57BL/6 mice, where they were retained for 14 days. After this period, spheres were harvested from euthanized mice and studied for cellular deposition and fibrosis (Fig. 1). Dark-field phase contrast images from retrieved spheres show a marked reduction in cellular deposition onto spheres as their size is increased (Fig. 1a). Cellular deposition on spheres was examined using Z-stacked confocal imaging using DAPI (nucleus marker), F-actin (cellular cytoskeleton marker) and α-smooth muscle actin (α-SMA, myofibroblast marker). Interestingly, the larger spheres had significantly reduced fibrotic deposition (Fig. 1b and Supplementary Fig. 2). Additional immunostaining for the host immune cell markers CD68 (macrophage), Ly6G/Ly6C-GR1 (neutrophil) and TGF-β (inflammation marker) also showed reduced immune cell deposition on larger spheres (Supplementary Fig. 3). qPCR expression analysis of additional fibrosis markers, namely collagen 1a1 (Col1a1), collagen 1a2 (Col1a2) and α-SMA, further indicated reduced cellular deposition as the sphere size was increased (Fig. 1c–e). Western blot analysis of α-SMA expression within the cellular overgrowth on spheres showed a significant decrease as sphere size was increased (Fig. 1f,g).

To ensure that the size-modulated fibrotic response effect is not simply a function of surface area, we implanted spheres of two sizes, 0.5 mm and 1.5 mm, normalized in total surface area. In other words, 100 µl/mouse of medium-sized and 300 µl/mouse of large-sized spheres were implanted into the intraperitoneal space of C57BL/6 mice and then retrieved after 14 days. Dark-field phase contrast images of the retrieved spheres revealed only limited cellular deposition on the 1.5-mm spheres and significant cellular deposition on the 0.5-mm spheres (Supplementary Fig. 4). These findings indicate that the phenomenon is size-mediated and independent of the total surface area of implanted material.

We next evaluated whether the effects of implant size on fibrosis are related to a delay in the kinetics of cellular deposition on the larger-sized spheres. To study this hypothesis, 0.3-mm and 1.5-mm SLG20 alginate hydrogel spheres were implanted into the intraperitoneal space of C57BL/6 mice for a significantly longer period of six months. After six months the implanted hydrogel spheres were retrieved and examined for cellular deposition. Dark-field phase contrast images from retrieved capsules show that the the 1.5-mm spheres are largely devoid of cellular deposition, whereas the 0.3-mm spheres are covered with deposited cells and are clumped together in fibrous tissue (Supplementary Fig. 5).

We also asked whether or not this size-modulated fibrotic deposition phenomenon would extend to other materials known to produce higher levels of fibrotic reactions on implantation. To this end, we implanted medium-sized (0.4–0.6 mm) and larger-sized (1.5–2.5 mm) spheres composed of SLG20 alginate (sterile-grade alginate), LF10/60 alginate (pharmaceutical-grade alginate), stainless steel, glass, polycaprolactone and polystyrene into the intraperitoneal space of C57BL/6 mice. The surface roughness of the material spheres we evaluated here included only relatively smooth-surfaced materials (<1 µm roughness)[32,33]. Bright-field images from retrieved materials 14 days post-implant revealed significant cellular deposition on the medium-sized versions of all materials tested. Interestingly, all materials tested at an increased size led to a marked reduction of the thickness of cellular overgrowth deposition (Fig. 2a). Immunofluorescence-stained z-stacked confocal images of retrieved materials show a significant decrease in macrophage (CD68) and myofibroblast (αSMA) deposition across all materials tested; significantly, large SLG20 alginate, LF10/60 (endotoxin containing alginate), glass and stainless steel spheres had negligible cellular deposition (Fig. 2b).

To further evaluate the innate immune response to spheres of different sizes, we collected and analysed the omental and epididymal fat pad tissue peripheral to the implants for innate immune cell infiltration, using a combination of flow cytometry (Fig. 2c,d) and qPCR analysis (Supplementary Fig. 6). These analyses revealed that across all materials tested (SLG20 alginate, LF10/60 alginate, stainless steel, glass, polycaprolactone and polystyrene) increasing sphere size led to a significant reduction of innate immune cell accumulation in peripheral tissue. These findings were further validated through a multiplexed inflammatory mouse cytokine profile (Fig. 2e). Notably, our evaluation of a spectrum of materials with a range of mechanical stiffness properties varying from soft (alginate hydrogels, <100 kPa; ref. 34) to hard (stainless steel, 100s of GPa; ref. 35) demonstrates that size and shape rather than stiffness plays a critical role in biocompatibility.

We next sought to examine whether this observed size-modulated fibrotic effect would translate to a larger rodent model. To examine this, we implanted 0.5-mm and 2.0-mm glass spheres into the intraperitoneal space of Sprague-Dawley rats and then retrieved the materials after 14 days. Bright-field and Z-stacked confocal images obtained from retrieved glass microspheres show that the large spheres are devoid of any cellular deposition, whereas the smaller spheres are significantly clumped together and embedded within a thick fibrotic capsule (Supplementary Fig. 7a,b).
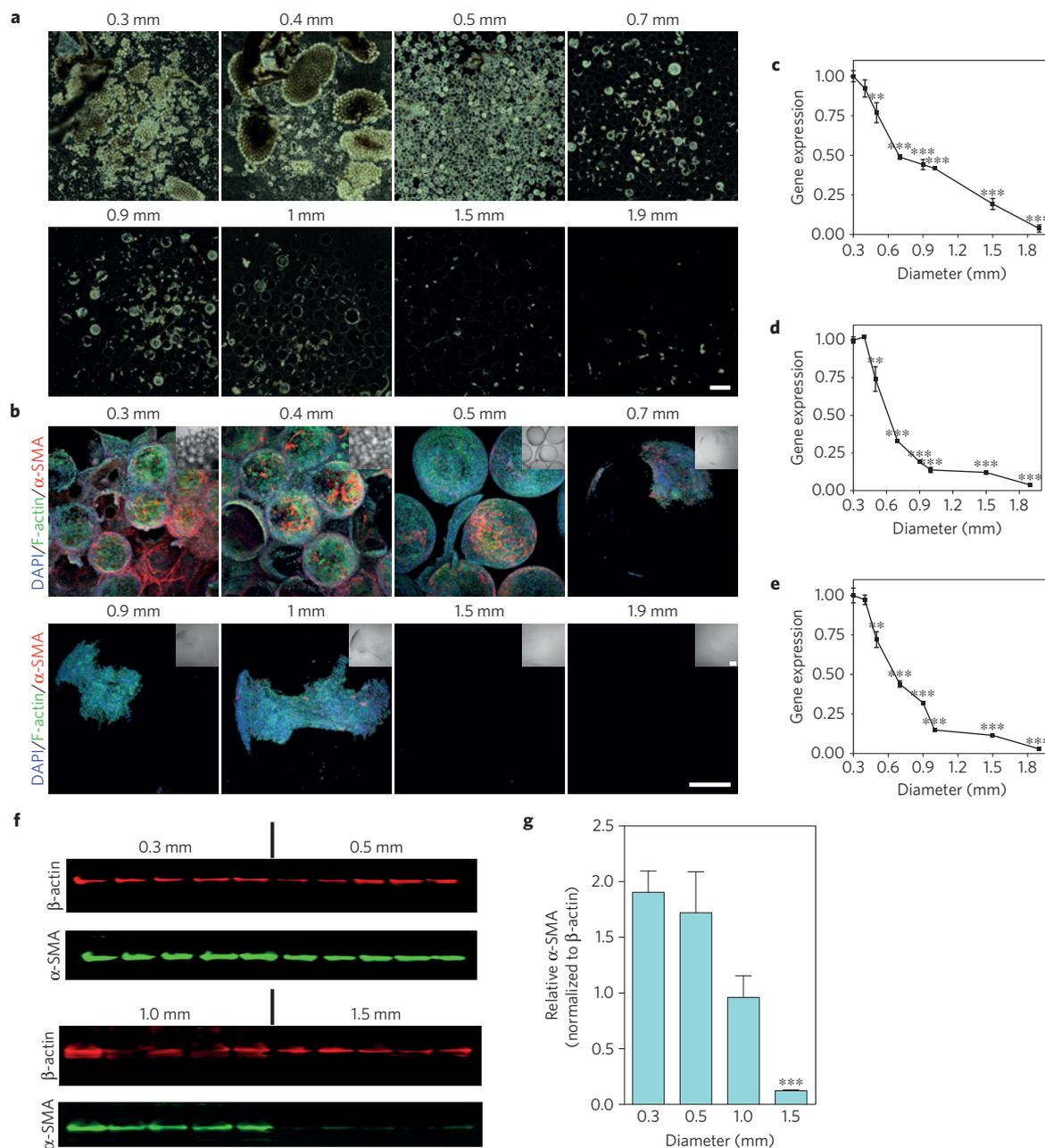
Figure 1 | Increasing alginate sphere size results in reduced cellular deposition and fibrosis formation on the spheres. SLG20 alginate spheres (0.5 ml in volume) of eight different sizes (0.3, 0.4, 0.5, 0.6, 0.7, 1, 1.5 and 1.9 mm) were implanted into the intraperitoneal space of C57BL/6 mice, where they were retained for 14 days and analysed for degree of fibrosis on retrieval. **a**, Dark-field phase contrast images obtained from retrieved spheres reveal a significant decrease in level of cellular overgrowth with increase in sphere size. Scale bar, 2 mm. **b**, Z-stacked confocal images of retrieved spheres immunofluorescence stained with DAPI (highlighting cellular nuclei), phalloidin (highlighting F-actin) and α-SMA (highlighting myofibroblast cells). Scale bar, 300 μm. **c–e**, qPCR-based expression analysis of fibrotic markers α-SMA (**c**), Collagen 1a1 (**d**, Col1a1) and Collagen 1a2 (**e**, Col1a2) directly on the eight different sphere sizes (0.3, 0.4, 0.5, 0.7, 0.9, 1, 1.5 and 1.9 mm) plotted normalized to relative expression levels on 300-μm spheres. **f**, Semiquantitative western blot analysis of α-SMA expression in cell overgrowth on microspheres. **g**, Plot of analysed band intensities from western blot images shown in **f**. Error bars, mean ± s.e.m. $N = 5$ mice per treatment. All experiments were performed at least three times. qPCR and western blot statistical analysis: one-way ANOVA with Bonferroni multiple comparison correction. **, $p < 0.001$; ***, $p < 0.0001$.

qPCR expression analysis of fibrosis markers, collagen 1a1 (Col1a1), collagen 1a2 (Col1a2) and αSMA, verified that increasing sphere size resulted in a significant reduction of fibrosis formation directly on spheres (Supplementary Fig. 7c). These results suggest our size-dependent fibrotic response observations in C57BL/6 mice also translate to other larger rodent species.

Next, we wanted to study if these findings could translate to higher-order species and also to other implant sites. To evaluate this, we implanted SLG20 alginate hydrogels, prepared as 0.5-mm and 1.5-mm spheres ($N = 4$) as well as cylinders (4 mm diameter × 1 mm height; $N = 2$), subcutaneously into the dorsal regions of non-human primates (NHPs) for either 14 or 28 days. At both 14 and 28 days post-implantation retrieval time points the 1.5-mm SLG20 alginate spheres were not embedded in host tissue and freely dissociated from the implant site on incision with a biopsy punch (Fig. 3a and Supplementary Fig. 8). The retrieved 1.5-mm
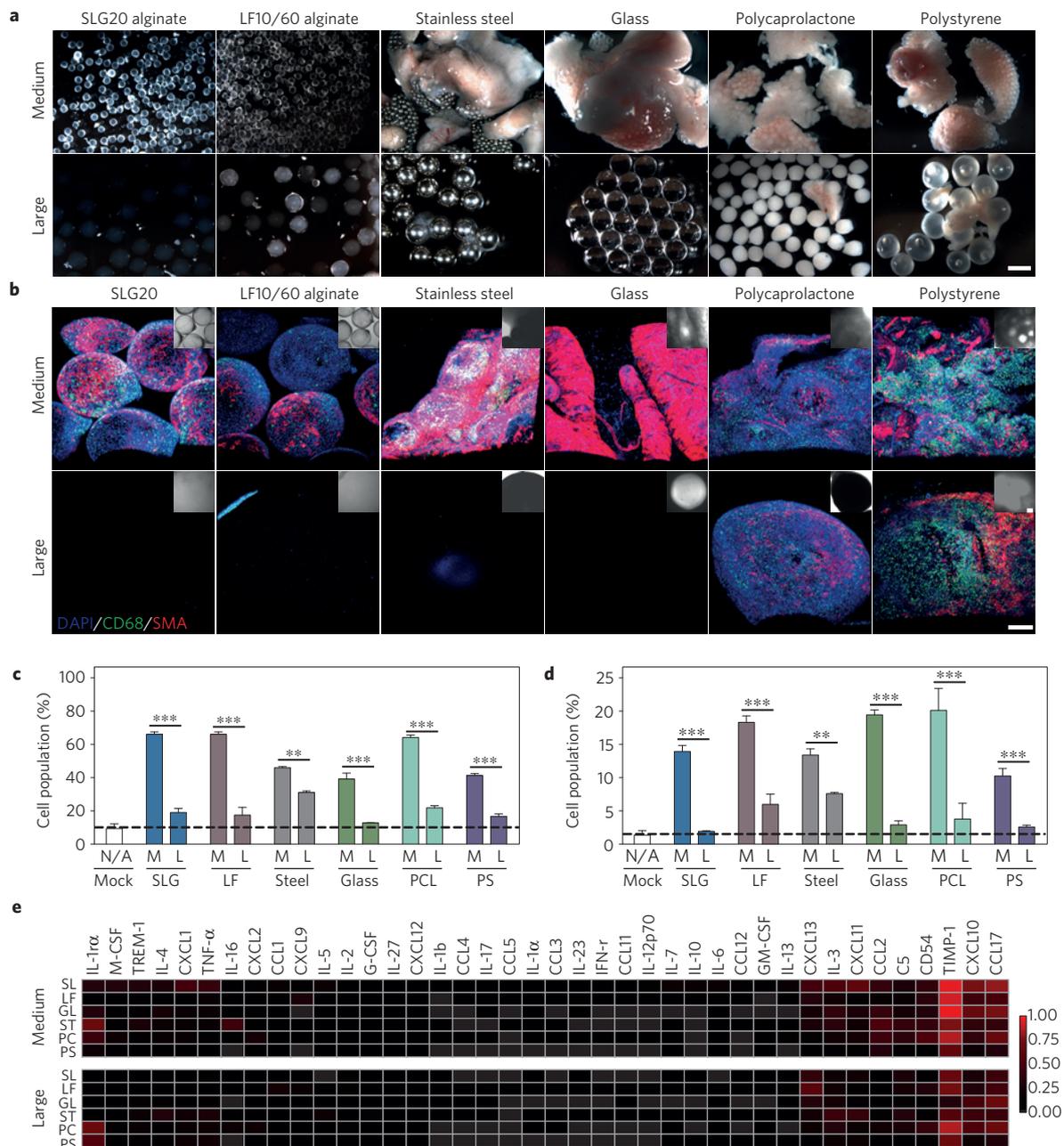
Figure 2 | Increasing the spherical diameter of a variety of materials, including, hydrogels, ceramics, metals and plastics, results in reduced foreign body responses. a, Bright-field images obtained from retrieved medium-sized (0.5 mm) and large-sized (1.5–2 mm) versions of SLG20 alginate, LF10/60 alginate (endotoxin containing), glass and polystyrene, 14 days post intraperitoneal implant into C57BL/6 mice. Scale bar, 2 mm. **b,** Panel of representative immunofluorescence Z-stacked confocal images of materials stained for cell nuclei (DAPI, blue), macrophages (CD68, green) and fibrosis-associated activated myofibroblasts (α-SMA, red). Scale bar, 300 μm. **c,d,** Flow analysis, using specific markers for responding host macrophage (**c**) and neutrophils (**d**). Mock, surgery and PBS-only injection; SLG, SLG20 alginate; LF, LF10/60 alginate (endotoxin containing); PCL, polycaprolactone; PS, polystyrene. **e,** Elispot multiplexed based cytokine array profiling of inflammatory cytokine protein production in response to implanted materials. SL, SLG20 alginate; LF, LF10/60 alginate (endotoxin containing); ST, stainless steel; GL, glass; PC, polycaprolactone; PS, polystyrene. Error bars, mean ± s.e.m. $N = 5$ mice per treatment. All experiments were performed at least three times. FACS size comparisons were performed by unpaired, two-tailed t-test. **, $p < 0.001$; ***, $p < 0.0001$.

spheres seemed visually to be translucent and devoid of cellular overgrowth (Fig. 3b and Supplementary Fig. 8). H&E stained sections of retrieved large spheres confirmed negligible cellular deposition and a lack of fibrosis (Fig. 3c). Conversely, at both 14- and 28-day retrieval time points, the implanted 0.5-mm spheres and cylinders were profusely embedded in host tissues (Supplementary Fig. 8). Excised tissue obtained from the implant sites of SLG20 alginate 1.5-mm spheres, 0.5-mm spheres, cylinders and saline-injected

control tissue were examined through histological analysis using a combination of H&E and Masson's Trichrome staining (Fig. 3d). The obtained images confirm the lack of large sphere embedding or fibrosis. However, extensive embedding and fibrosis build-up (up to 100 μm thick) is visible, enveloping the implanted cylinders and medium-sized spheres.

To confirm that the subcutaneous dorsal NHP observations could also translate to the intraperitoneal site of NHPs, a smaller
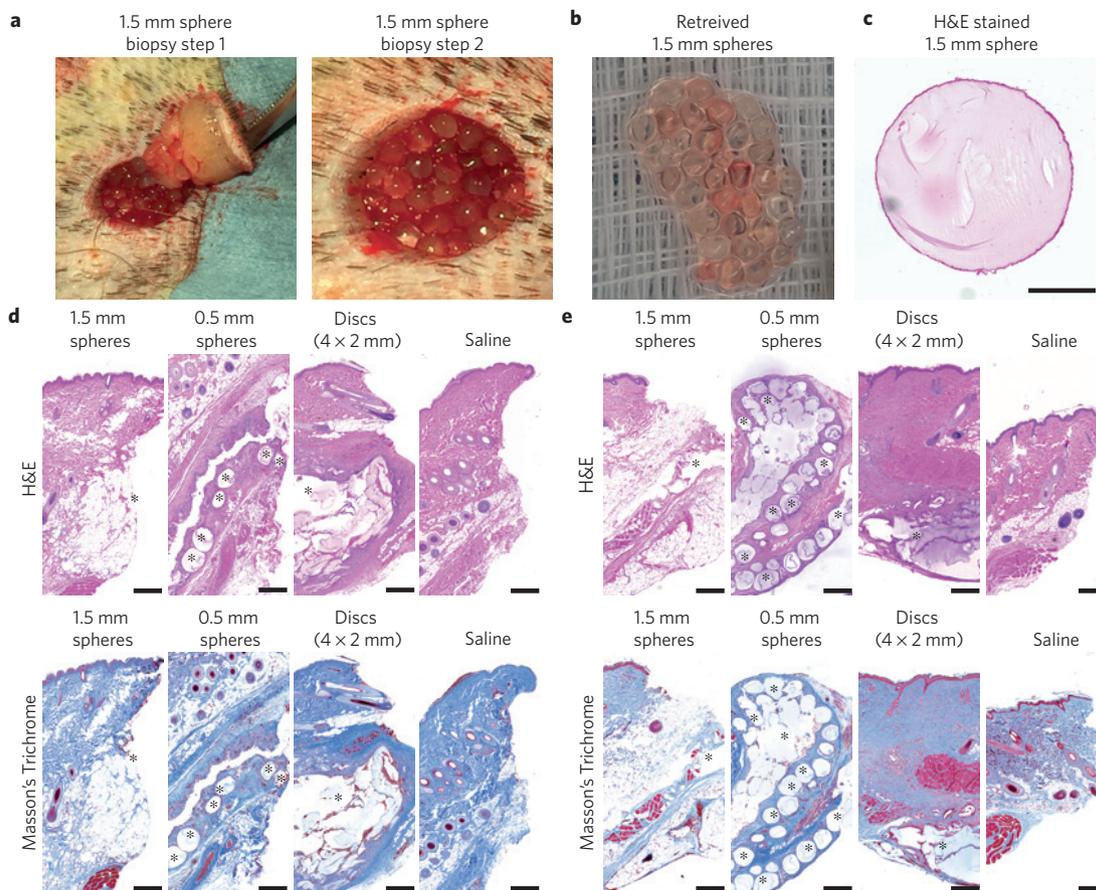
Figure 3 | Comparing the size- and shape-dependent effects of fibrosis formation on alginate hydrogels implanted in the subcutaneous dorsal region of non-human primates. a, Large (1.5 mm in diameter) spheres of SLG20 hydrogels implanted subcutaneously in the dorsal region of cynomolgus macaque resist fibrosis, whereas small spheres (0.5 mm in diameter) and cylinders (4 mm in diameter and 2 mm in height) become fibrotic. After 14 days, biopsy punches were used to excise implanted materials/peripheral host tissue; on incision we observed that the large SLG20 alginate spheres were not embedded in host tissue and freely dissociated from the implant site. **b,c**, The retrieved large SLG20 hydrogels visually seem to be transparent and devoid of cellular deposition (**b**), which was also confirmed using H&E stained histological analysis (**c**; scale bar, 500 μm). **d,e**, H&E and Masson's Trichrome stained histological sections of excised tissue at 14 days (**d**) and 28 days (**e**) post-implantation with SLG20 alginate hydrogels formed onto large spheres (1.5 mm in diameter), medium spheres (0.5 mm in diameter) or cylinders (4 mm in diameter and 1 mm in height), as well as a control saline-alone injection (* in images demarcates the implanted materials). Scale bars, 500 μm. $N = 2$ for saline and discs; $N = 4$ for both 0.5-mm and 1.5-mm sphere groups. These experiments were performed once.

pilot study was performed, in which 0.5-mm and 1.5-mm spheres of SLG20 alginate hydrogels were separately implanted into non-human primates ($n = 1$ per treatment) using a minimally invasive laparoscopic procedure (Supplementary Fig. 9)[36]. A laparoscopic camera was used to capture images and video of the spheres immediately after, and again at 14 days post-implantation. The obtained *in situ* images reveal that the 1.5-mm spheres remain translucent and are not embedded into host omentum/fat tissue after 14 days; conversely, the 0.5-mm spheres are impeded in to the omentum/fat tissue (Supplementary Fig. 9a). An IP lavage with saline at 14 days post-implantation enabled retrieval of SLG20 1.5-mm spheres; however, the 0.5-mm spheres could not be retrieved because of strong adherence and embedding into the IP host tissue (omentum) (Supplementary Movies 1 and 2). The retrieved 1.5-mm spheres were examined using dark-field imaging and seem to be transparent with negligible cellular overgrowth (Supplementary Fig. 9b). Z-stacked confocal imaging of the retrieved 1.5-mm spheres confirms minimal cellular deposition, a lack of immune macrophages, and fibrosis-associated activated myofibroblast coverage (Supplementary Fig. 9c). To verify the embedding of the 0.5-mm spheres within the NHP omentum, a biopsy punch was used to excise a sample of this tissue

for histological analysis, which confirmed their embedding, and significant fibrotic tissue build-up was observed enveloping the medium-sized spheres (Supplementary Fig. 9d).

To highlight the implications of our findings we investigated whether the improvements we observed in biocompatibility through the tuning of material geometry could produce improved/prolong function of an implanted biomedical device. To study this effect, we evaluated the survival of islets of Langerhans (islets) immunoiso-lated/encapsulated within conventionally sized 0.5-mm alginate microcapsules compared against islets protected within a 1.5-mm capsule. Previously, we and others have shown that host recognition and fibrosis via cellular and collagen deposition on the surface of transplanted 0.5-mm alginate microcapsules results in encapsulated islet graft cell death and the failure of diabetic correction in STZ-treated C57BL/6 mice[28,37,38]. Notably, in the context of islet encapsulation, the diameter of the hydrogel capsules is a parameter that has been largely overlooked, and based on our observations it could play an important role in improving the efficacy of the transplanted grafts[39]. Furthermore, it has been traditionally assumed that small capsules (<350 μm) allow better diffusion and transportation of nutrients and oxygen to the encapsulated islets than medium (350–700 μm) and larger capsules (>700 μm; ref. 40). Thus, to our knowledge
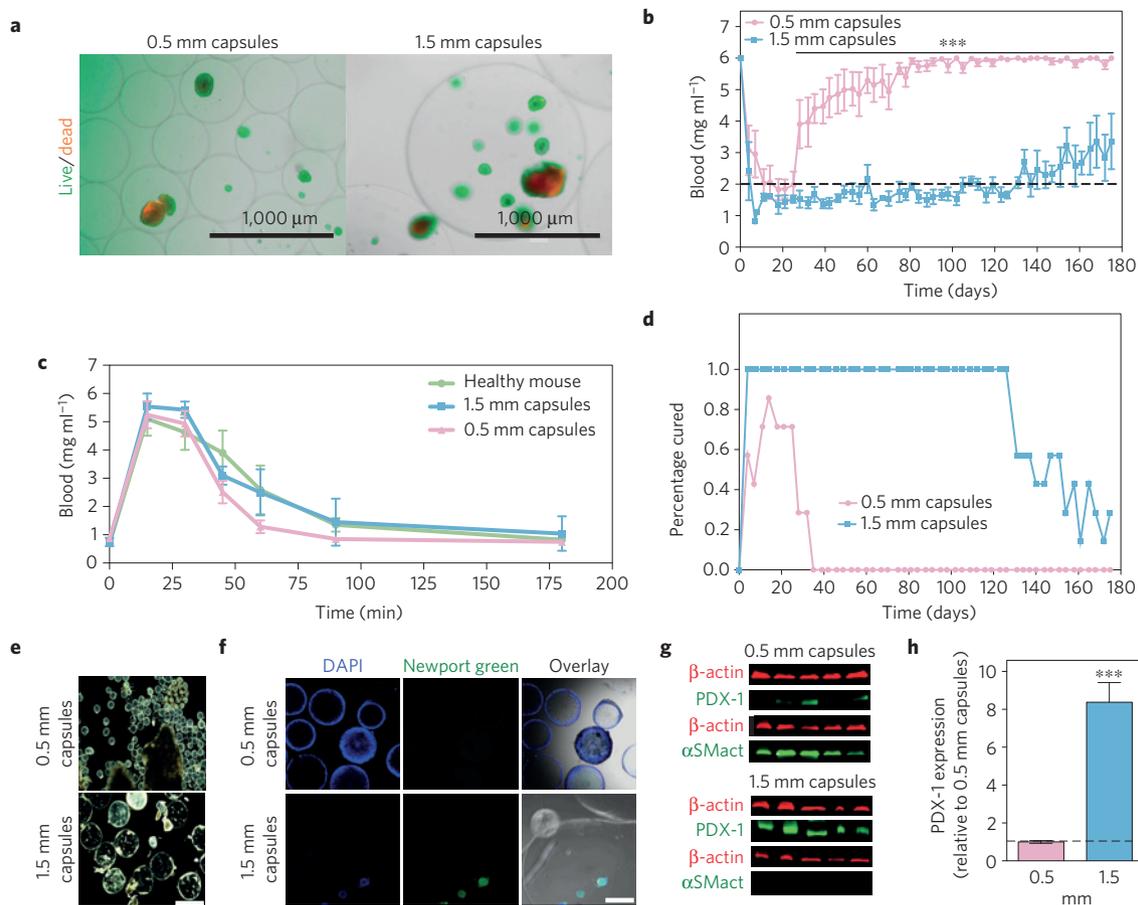
Figure 4 | Comparison of 0.5 and 1.5-mm alginate capsules encapsulating rat islets (500 IEs) in curing STZ-induced C57BL/6 diabetic mice. a, Live/dead staining confirming the viability of islet cells post-encapsulation for large (1.5-mm) as well as standard (0.5-mm) capsules. **b**, Blood-glucose curves showing prolonged normoglycaemia with large (1.5-mm) hydrogel alginate capsules, but only short-lived success with standard (0.5-mm) capsules. **c**, *In vivo* glucose tolerance test (iv GTT) of healthy mice and diabetic mice seven days post-transplantation with rat islets encapsulated in standard (0.5-mm) or large (1.5-mm) capsules shows no significant delays in BG correction as a function of capsule geometry. **d**, Kaplan–Meier plot showing the fraction of cured STZ-C57BL/6 mice after being transplanted with either 0.5-mm or 1.5-mm capsules, containing 500 IEs of primary rat islets. **e**, Representative dark-field phase contrast images of retrieved 0.5-mm or 1.5-mm alginate islet-containing capsules six months after transplantation show higher levels of cellular overgrowth on 0.5-mm capsules. Scale bar, 2,000 μm. **f**, Confocal imaging panel showing nuclear DAPI, Newport green (islet marker), and overlay with bright-field images of visible capsules. Scale bar, 300 μm. **g**, Rat PDX-1 and host α-SMA expression from capsules retrieved from STZ-treated mice 175 days post-transplant. As a reference, β-actin expression levels are also shown. **h**, qPCR analysis of rat islet marker PDX-1 expression in retrieved 0.5-mm or 1.5-mm alginate capsules. Error bars, mean ± s.e.m. $N = 5$ mice per treatment. All experiments were performed at least two or three times. qPCR statistical analysis: one-way ANOVA with Bonferroni multiple comparison correction ***, $p < 0.0001$.

larger 1.5-mm spherical capsules have previously not been evaluated for islet cell encapsulation.

Using a xenogeneic treatment model of transplanting rat pancreatic islets into STZ-induced diabetic C57BL/6 mice, we investigated the role of capsule size on cell survival. Rat islets (500 IEs per mouse) were separately encapsulated into SLG20 alginate hydrogels, prepared as 1.5-mm or 0.5-mm spheres. For these studies we used an islet density preparation of 500 IEs per 0.325 ml alginate solution because at this density we observed very few protrusions of islets outside of capsules. Live/dead staining was used to confirm the viability of islets after encapsulation (Fig. 4a). To investigate potential diffusion barriers due to using larger-sized 1.5-mm capsules, before transplantation we evaluated the kinetics of both glucose and insulin diffusion within 1.5-mm and 0.5-mm capsules loaded with islets. We observed no significant differences in diffusion kinetics of glucose (Supplementary Fig. 10) or insulin (Supplementary Fig. 11) as a function of capsule geometry (Supplementary Discussion). After transplantation, blood-glucose (BG) correction was used as an indicator to non-invasively monitor cell graft function over time, and measurements were taken at

least three times a week. All mice ($n = 5$) in the 0.5-mm capsule group failed (that is, BG above 2 mg ml⁻¹ for three consecutive measurements), on average, by 30 days following transplantation, whereas in the 1.5-mm capsule group ($n = 5$) the mice stayed cured, on average, even until 175 days (a greater than five times increase) post-transplantation, when the experiment was stopped (Supplementary Fig. 12). The difference in both BG normalization (Fig. 4b) and fraction cured (Fig. 4d) was significantly different ($p < 0.0001$) between the 0.5-mm and 1.5-mm capsule groups following the initial failure in regulating BGs by the 0.5-mm group (∼day 25) throughout the remainder of the experiment. At seven days post-transplantation a glucose tolerance test (GTT) was used to evaluate the kinetics of blood-glucose correction, and no significant delays were measured as a function of capsule geometry (Fig. 4c).

On termination of this study, six months post-transplantation, capsules were retrieved and analysed for fibrosis and the presence of viable islets. Dark-field imaging revealed that the 0.5-mm capsules were covered in cellular deposition and clumped, whereas the 1.5-mm capsules were largely clean and devoid of cellular deposition (Fig. 4e). Confocal images acquired from retrieved 0.5-mm and
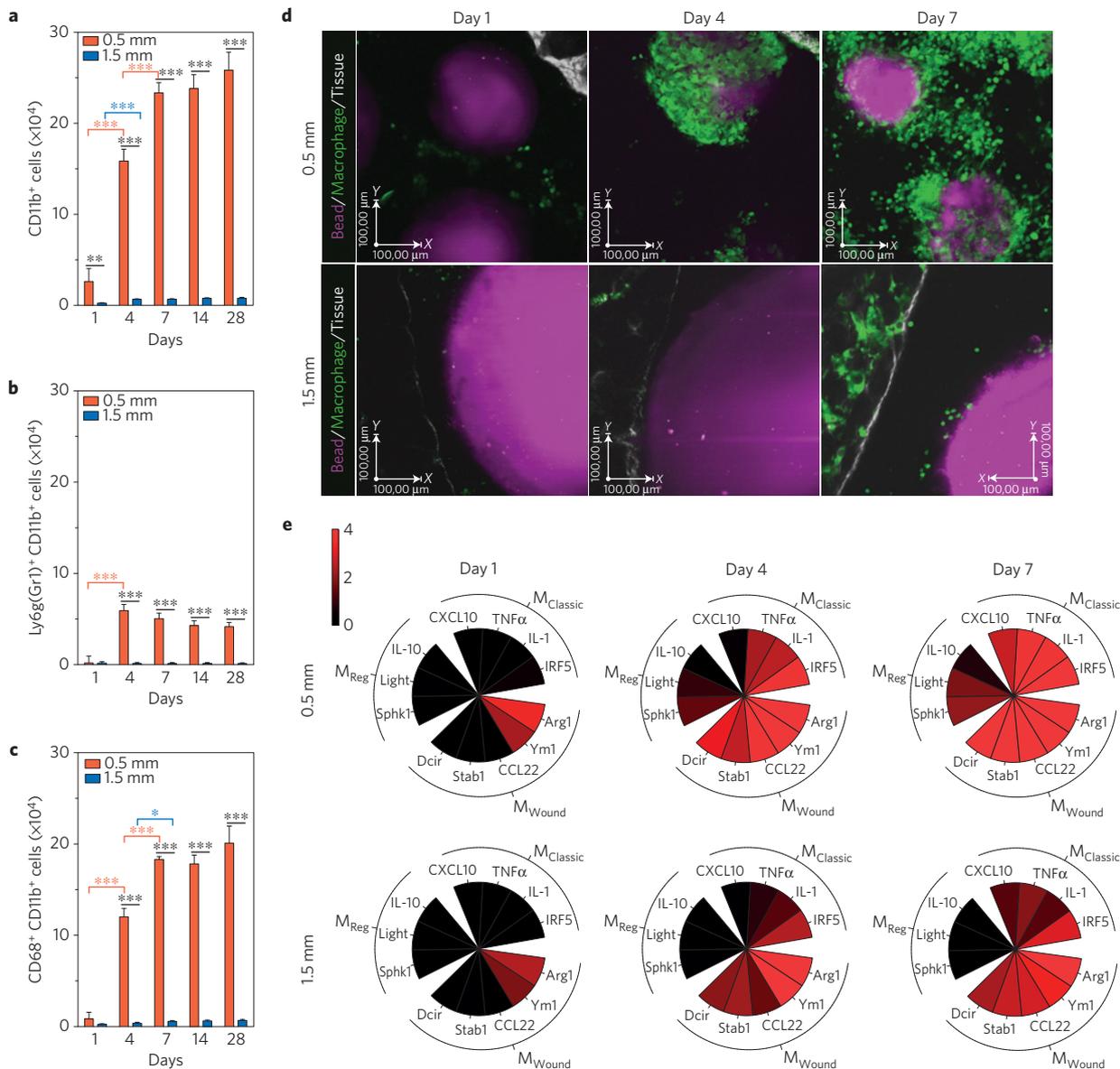
Figure 5 | Kinetic profiling of host response to SLG20 alginate microspheres of diameter 0.5 and 1.5 mm. a–c, Flow analysis, using specific markers for responding host innate immune myeloid (**a**), neutrophil (**b**), and macrophage cells (**c**) at 1, 4, 7, 14 and 28 days post-implantation. **d**, *In vivo* intravital imaging of macrophage behaviour and accumulation at 1, 4, or 7 days post-implantation. **e**, NanoString-based analysis for expression of macrophage phenotype markers analysed from deposited cell RNA extracts at 1, 4 and 7 days post-implant, presented on a base 2 logarithmic scale. Error bars, mean ± s.e.m. For FACS analysis, $N = 5$ mice per treatment; for intravital imaging, $N = 3$ mice per treatment; for NanoString analysis, $N = 4$ per treatment. FACS and intravital imaging experiments were performed twice and NanoString analysis was performed once. FACS size comparisons were performed by unpaired, two-tailed *t*-test. *, $p < 0.05$; **, $p < 0.001$; ***, $p < 0.0001$. For NanoString statistical analyses see Supplementary Methods.

1.5-mm capsules showed positive Newport Green (islet viability marker) staining only in the 1.5-mm capsule group (Fig. 4f). Western blot assays were also performed on extracted proteins from retrieved capsules in each group to monitor relative expression of PDX-1 (islet viability marker) and α-SMA (fibrosis marker). For this assay, approximately 50% of capsules retrieved from each mouse was digested and processed for total protein extraction. Four out of five mice in the 0.5-mm capsule group had comparatively diminished PDX-1 expression and all five mice showed high levels of α smooth muscle expression; conversely, high levels of PDX-1 and minimal α-SMA were detected in capsules retrieved from all five mice in the 1.5-mm capsule group (Fig. 4g). PDX-1 expression results were further verified using qPCR analysis of RNA isolated from retrieved capsules, and approximately eight times higher levels of rat PDX-1 were detectable in the 1.5 mm capsules compared with the 0.5-mm

capsule group (Fig. 4h). Taken in combination, our results suggest that grafts in 1.5-mm capsules survived approximately six times longer than those prepared in conventionally sized 0.5-mm capsules because the tuned geometry hydrogels were able to resist fibrosis for a longer duration. Interestingly, although we did not observe significant build-up of fibrosis on the capsules on retrieval after 180 days, the mice in this treatment group lost blood-glucose control after approximately 140 days. This possibly suggests some islet viability loss after transplantation, which could be related to the long-term durability of the rat islets used in this treatment model.

To better understand innate immune response as a function of implant size, we conducted a kinetic profiling analysis of host-mediated innate immune recognition following implantation of 0.5-mm and 1.5-mm SLG20 alginate spheres, over a 28-day period (Fig. 5) in C57BL/6 mice. Flow cytometry was used to quantify the

accumulation of myeloid cells (Fig. 5a), neutrophils (Fig. 5b) and macrophages (Fig. 5c) directly on spheres of 0.5-mm and 1.5-mm sizes at 1, 4, 7, 14 and 28 days post-implant. At all time points evaluated, we observed a significant increase in the accumulation of myeloid cells onto 0.5-mm spheres compared with the 1.5-mm spheres (Fig. 5a). In probing macrophage and neutrophil cells, by four days post-implantation we observed significantly increased accumulation on 0.5-mm spheres, which appears to plateau by day 7 (Fig. 5b,c). Notably, on 1.5-mm spheres we observed negligible numbers of neutrophil cells and a limited number of myeloid and macrophage cells at all time points.

Macrophages have been implicated as key drivers of the foreign body reaction to implanted materials[41]. To probe their role towards the fibrotic responses to the implanted materials we performed a series of experiments in which we transplanted SLG20 alginate spheres into the IP space of a transgenic mouse model, MAFIA, which enables the induction of macrophage cell depletion. In this model, a macrophage Fas cell surface death receptor (Fas)-induced apoptosis transgene enables inducible/reversible apoptosis of macrophages using the mouse colony stimulating factor 1 receptor promoter (CSF1R) to drive expression of a mutant human FK506 binding protein 1A, 12 kDa (ref. 42). Furthermore, an EGFP transgene included in this model enables the *in situ* fluorescent monitoring of macrophage cells[42].

First, to confirm the importance of macrophages in driving the fibrosis responses we transplanted 0.5-mm SLG20 spheres into the IP space of MAFIA mice treated to induce depletion of macrophages and also as a control into MAFIA mice without depletion for 14 days. Dark-field microscope images of the retrieved spheres revealed only limited cellular deposition onto spheres implanted in mice with depleted macrophages, and conversely significant cellular deposition onto spheres received from mice with macrophages (Supplementary Fig. 13). These results confirm that macrophages are indeed a key driver of the fibrotic responses we have observed in response to our transplanted materials.

Second, to monitor macrophage behaviour in real time, we performed *in vivo* intravital imaging on implanted alginate spheres of 0.5 mm and 1.5 mm in size, which were fluorescently labelled. Spherical implants were studied in the IP space of MAFIA mice (Supplementary Fig. 14). *In vivo* Z-stacked intravital images obtained from implanted medium- and large-sized spheres at 1, 4 and 7 days post-implant indicate that macrophage cells extravasate from peripheral fat pad tissue and accumulate onto 0.5-mm spheres over that one-week period, whereas very few macrophages can be observed near the 1.5-mm spheres (Fig. 5d). Z-stacked and time lapse intravital images of macrophage accumulation onto 0.5-mm and 1.5-mm spheres at 1, 4 and 7 days post-implantation confirm both a lack of macrophage activity and numbers surrounding 1.5-mm spheres, and significant macrophage activity and numbers around 0.5-mm spheres (Supplementary Movies 3–8). We hypothesized that because the 1.5-mm spheres are surrounded by only a few macrophage cells, the macrophages around the large spheres are not becoming activated, resulting in reduced recruitment and extravasation of additional macrophages.

Macrophage cells have remarkable plasticity that allows them to efficiently respond to environmental signals and change their phenotype to address the implicated stimuli[43]. There is a broad spectrum of macrophage activations, which can be categorized into three states: namely, classical activation (pro-inflammatory, $M_{Classic}$), alternative activation (pro-healing, M_{Wound}) and regulatory activation (M_{Reg}; ref. 44). These phenotypes can be characterized through gene expression analysis of specific markers that correlate with each activation state[45]. A pro-inflammatory macrophage phenotype correlates with elevated expression of tumour necrosis factor α (TNF-α), interleukin 1 (IL-1), and interferon regulatory factor 5 (IRF5; refs 44–46). A pro-wound-healing phenotype of

macrophage correlates with upregulation in expression of dendritic cell immune receptor (Dcir), stabilin 1 (Stab1), chemokine (C-C motif) ligand 22 (CCL22), chitinase-like 3 (YM1), and arginase 1 (Arg1; refs 44–46). Meanwhile, a regulatory macrophage phenotype has been characterized to correlate with elevated expression of interleukin 10 (IL-10), TNF superfamily member 14 (Light) and sphingosine kinase 1 (Sphk1; refs 44–46). To elucidate the changing activation/differentiation states of macrophages we examined a range of implanted constructs using a series of markers reflecting $M_{Classic}$, M_{Wound} and M_{Reg} phenotypes[41,43,44,46]. At 1, 4 and 7 days post-implantation, gene expression analysis was used to probe phenotype marker expression of cells isolated from the intraperitoneal space, omental fat pad tissue, and directly on spheres. Overall, we observed significantly different gene expression patterns for cells associated with these tissues following implantation of 0.5-mm spheres when compared with 1.5-mm spheres (Supplementary Table 1).

Implantation of both 0.5-mm and 1.5-mm spheres resulted in an increased expression of markers associated with a wound-healing phenotype in the intraperitoneal and peripheral omentum fat compartments (Supplementary Figs 15 and 16, and Supplementary Table 1). This phenotype was elevated at day 4 for both sizes of spheres implanted in mice, and decreased by day 7 for the 1.5-mm spheres. We believe that these data are consistent with macrophage activation in these compartments—that is, reduced when the implanted material consists of 1.5-mm spheres. Fibrotic tissue obtained directly from the 0.5-mm spheres showed increasing expression of markers associated with all three macrophage phenotypes. In contrast, expression of macrophage markers associated only with classical and wound-healing phenotypes was enriched in 1.5-mm spheres (Fig. 5e and Supplementary Table 1). Regulatory macrophage markers were not significantly upregulated at any time point or in any compartment tested following implantation of 1.5-mm spheres. However, increased expression of markers associated with this macrophage phenotype was observed on days 4 and 7 in cells associated with the 0.5-mm spheres (Fig. 5e). Combined our observations suggest that a lack of regulatory macrophage cell accumulation on large-sized spheres correlates with the truncated fibrosis responses.

In summary, we have demonstrated that by tuning the geometry of implanted materials we can influence their host recognition and propagation of foreign body reactions. Spherical materials that are of 1.5 mm in diameter or greater proved to be significantly more biocompatible than their smaller-sized or differently shaped counterparts. This effect was demonstrated to be independent of total implanted surface area and visible with all materials tested. Further, our finding suggests that simply increasing implant size is insufficient to resist foreign body responses, and that a spherical shape is also integral in resisting host fibrosis/rejection. Significantly, alginate microspheres of 1.5 mm in diameter demonstrated an ability to ward off cellular deposition for at least six months. Modulating the spherical dimensions of a broad spectrum of materials, encompassing hydrogels, ceramics, metals and plastics, also showed that spheres of 1.5 mm in diameter or greater significantly mitigated foreign reactions and fibrosis. We believe that these findings have important implications for the design of *in vivo*-implanted biomedical devices for a range of applications, including cell transplantation, controlled drug release, implantable sensors, and prosthesis for tissue engineering.

Methods

Methods and any associated references are available in the online version of the paper.

References

1. Kearney, C. J. & Mooney, D. J. Macroscale delivery systems for molecular and cellular payloads. *Nature Mater.* **12**, 1004–1017 (2013).
2. Farra, R. *et al.* First-in-human testing of a wirelessly controlled drug delivery microchip. *Sci. Transl. Med.* **4**, 122ra121 (2012).
3. Nichols, S. P., Koh, A., Storm, W. L., Shin, J. H. & Schoenfisch, M. H. Biocompatible materials for continuous glucose monitoring devices. *Chem. Rev.* **113**, 2528–2549 (2013).
4. Rosen, M. R., Robinson, R. B., Brink, P. R. & Cohen, I. S. The road to biological pacing. *Nature Rev. Cardiol.* **8**, 656–666 (2011).
5. Hubbell, J. A. & Langer, R. Translating materials design to the clinic. *Nature Mater.* **12**, 963–966 (2013).
6. Franz, S., Rammelt, S., Scharnweber, D. & Simon, J. C. Immune responses to implants—a review of the implications for the design of immunomodulatory biomaterials. *Biomaterials* **32**, 6692–6709 (2011).
7. Anderson, J. M., Rodriguez, A. & Chang, D. T. Foreign body reaction to biomaterials. *Semin. Immunol.* **20**, 86–100 (2008).
8. Williams, D. F. On the mechanisms of biocompatibility. *Biomaterials* **29**, 2941–2953 (2008).
9. Ratner, B. D. Reducing capsular thickness and enhancing angiogenesis around implant drug release systems. *J. Control. Release* **78**, 211–218 (2002).
10. Bryers, J. D., Giachelli, C. M. & Ratner, B. D. Engineering biomaterials to integrate and heal: The biocompatibility paradigm shifts. *Biotechnol. Bioeng.* **109**, 1898–1911 (2012).
11. Zhang, L. *et al.* Zwitterionic hydrogels implanted in mice resist the foreign-body reaction. *Nature Biotechnol.* **31**, 553–556 (2013).
12. Smith, R. S. *et al.* Vascular catheters with a nonleaching poly-sulfobetaine surface modification reduce thrombus formation and microbial attachment. *Sci. Transl. Med.* **4**, 153ra132 (2012).
13. Ma, M. *et al.* Development of cationic polymer coatings to regulate foreign-body responses. *Adv. Mater.* **23**, H189–H194 (2011).
14. Rodriguez, P. L. *et al.* Minimal "Self" peptides that inhibit phagocytic clearance and enhance delivery of nanoparticles. *Science* **339**, 971–975 (2013).
15. Kim, Y. K., Que, R., Wang, S. W. & Liu, W. F. Modification of biomaterials with a self-protein inhibits the macrophage response. *Adv. Healthc. Mater.* **3**, 989–994 (2014).
16. Madden, L. R. *et al.* Proangiogenic scaffolds as functional templates for cardiac tissue engineering. *Proc. Natl Acad. Sci. USA* **107**, 15211–15216 (2010).
17. Kusaka, T. *et al.* Effect of silica particle size on macrophage inflammatory responses. *PLoS ONE* **9**, e92634 (2014).
18. Zandstra, J. *et al.* Microsphere size influences the foreign body reaction. *Eur. Cells Mater.* **28**, 335–347 (2014).
19. Matlaga, B. F., Yasenchak, L. P. & Salthouse, T. N. Tissue response to implanted polymers: The significance of sample shape. *J. Biomed. Mater. Res.* **10**, 391–397 (1976).
20. Salthouse, T. N. Some aspects of macrophage behavior at the implant interface. *J. Biomed. Mater. Res.* **18**, 395–401 (1984).
21. Helton, K. L., Ratner, B. D. & Wisniewski, N. A. Biomechanics of the sensor-tissue interface-effects of motion, pressure, and design on sensor performance and the foreign body response-part I: Theoretical framework. *J. Diabetes Sci. Technol.* **5**, 632–646 (2011).
22. Brauker, J. H. *et al.* Neovascularization of synthetic membranes directed by membrane microarchitecture. *J. Biomed. Mater. Res.* **29**, 1517–1524 (1995).
23. Ward, W. K., Slobodzian, E. P., Tiekotter, K. L. & Wood, M. D. The effect of microgeometry, implant thickness and polyurethane chemistry on the foreign body response to subcutaneous implants. *Biomaterials* **23**, 4185–4192 (2002).
24. Lee, K. Y. & Mooney, D. J. Alginate: Properties and biomedical applications. *Prog. Polym. Sci.* **37**, 106–126 (2012).
25. Whelehan, M. & Marison, I. W. Microencapsulation using vibrating technology. *J. Microencapsulation* **28**, 669–688 (2011).
26. Lim, F. & Sun, A. M. Microencapsulated islets as bioartificial endocrine pancreas. *Science* **210**, 908–910 (1980).
27. Scharp, D. W. & Marchetti, P. Encapsulated islets for diabetes therapy: History, current progress, and critical issues requiring solution. *Adv. Drug Deliv. Rev.* **67–68**, 35–73 (2014).
28. Dolgin, E. Encapsulate this. *Nature Med.* **20**, 9–11 (2014).
29. Dang, T. T. *et al.* Spatiotemporal effects of a controlled-release anti-inflammatory drug on the cellular dynamics of host response. *Biomaterials* **32**, 4464–4470 (2011).
30. King, A., Sandler, S. & Andersson, A. The effect of host factors and capsule composition on the cellular overgrowth on implanted alginate capsules. *J. Biomed. Mater. Res.* **57**, 374–383 (2001).
31. Kolb, M. *et al.* Differences in the fibrogenic response after transfer of active transforming growth factor-β1 gene to lungs of "fibrosis-prone" and "fibrosis-resistant" mouse strains. *Am. J. Respir. Cell Mol. Biol.* **27**, 141–150 (2002).

32. Lekka, M., Sainz-Serp, D., Kulik, A. J. & Wandrey, C. Hydrogel microspheres: Influence of chemical composition on surface morphology, local elastic properties, and bulk mechanical characteristics. *Langmuir* **20**, 9968–9977 (2004).
33. Shellenberger, K. & Logan, B. E. Effect of molecular scale roughness of glass beads on colloidal and bacterial deposition. *Environ. Sci. Technol.* **36**, 184–189 (2002).
34. Papajova, E., Bujdos, M., Chorvat, D., Stach, M. & Lacik, I. Method for preparation of planar alginate hydrogels by external gelling using an aerosol of gelling solution. *Carbohydr. Polym.* **90**, 472–482 (2012).
35. Fujie, T. *et al.* Evaluation of substrata effect on cell adhesion properties using freestanding poly(L-lactic acid) nanosheets. *Langmuir* **27**, 13173–13182 (2011).
36. Qi, M. *et al.* A recommended laparoscopic procedure for implantation of microcapsules in the peritoneal cavity of non-human primates. *J. Surg. Res.* **168**, e117–e123 (2011).
37. Dang, T. T. *et al.* Enhanced function of immuno-isolated islets in diabetes therapy by co-encapsulation with an anti-inflammatory drug. *Biomaterials* **34**, 5792–5801 (2013).
38. de Groot, M., Schuurs, T. A. & van Schilfgaarde, R. Causes of limited survival of microencapsulated pancreatic islet grafts. *J. Surg. Res.* **121**, 141–150 (2004).
39. Strand, B. L., Gaserod, O., Kulseng, B., Espevik, T. & Skjak-Baek, G. Alginate-polylysine-alginate microcapsules: Effect of size reduction on capsule properties. *J. Microencapsulation* **19**, 615–630 (2002).
40. Robitaille, R. *et al.* Studies on small (<350 microm) alginate-poly-L-lysine microcapsules. III. Biocompatibility Of smaller versus standard microcapsules. *J. Biomed. Mater. Res.* **44**, 116–120 (1999).
41. Shi, C. & Pamer, E. G. Monocyte recruitment during infection and inflammation. *Nature Rev. Immunol.* **11**, 762–774 (2011).
42. Burnett, S. H. *et al.* Conditional macrophage ablation in transgenic mice expressing a Fas-based suicide gene. *J. Leukocyte Biol.* **75**, 612–623 (2004).
43. Gordon, S. Alternative activation of macrophages. *Nature Rev. Immunol.* **3**, 23–35 (2003).
44. Mosser, D. M. & Edwards, J. P. Exploring the full spectrum of macrophage activation. *Nature Rev. Immunol.* **8**, 958–969 (2008).
45. Murray, P. J. *et al.* Macrophage activation and polarization: Nomenclature and experimental guidelines. *Immunity* **41**, 14–20 (2014).
46. Gordon, S. & Martinez, F. O. Alternative activation of macrophages: Mechanism and functions. *Immunity* **32**, 593–604 (2010).

Author contributions

O.V., J.C.D., M.M. and D.G.A. conceived the idea, designed experiments, analysed data, and wrote the manuscript. O.V., J.C.D., M.M. A.J.V., A.R.B., J.L., E.L., J.W., W.S.L., S.J., A.C., S.S., K.T., J.H-L., S.A-D., M.B., J.M-E., Y.W., M.Q., D.M.L., M.C., N.D., R.T., I.L., G.C.W. and J.O. performed experiments. H.H.T. performed statistical analyses of data sets and aided in the preparation of displays communicating data sets. G.C.W., J.O. and D.L.G. provided conceptual advice and technical support. R.L. and D.G.A. supervised the study. All authors discussed the results and assisted in the preparation of the manuscript.

Additional information

Supplementary information is available in the online version of the paper. Reprints and permissions information is available online at www.nature.com/reprints. Correspondence and requests for materials should be addressed to D.G.A.

Competing financial interests

The authors declare no competing financial interests.

Methods

Detailed description of methods and any associated references are available in the online version of the paper. In brief, all materials were implanted intraperitoneally or subcutaneously into and retrieved at specified times from C57BL/6 mice, C57BL/6-Tg(CSF1R-EGFP-NGFR/FKBP1A/TNFRSF6)2Bck/J mice, Sprague-Dawley rats, or cynomolgus macaque non-human primates in accordance with approved protocols and federal guidelines. Sample processing, staining, FACS, NanoString expression analysis and imaging were performed as detailed in the Supplementary Information. Shown are representative images from at minimum $n = 5$ mice per treatment group. For rat studies, $n = 3$ per treatment. Quantified data shown are group mean values $\pm$ s.e.m. References cited in the Supplementary Information[47–51].

References

47. Lacy, P. E. & Kostianovsky, M. Method for the isolation of intact islets of Langerhans from the rat pancreas. *Diabetes* **16,** 35–39 (1967).
48. Morch, Y. A., Donati, I., Strand, B. L. & Skjak-Braek, G. Effect of Ca2+, Ba2+, and Sr2+ on alginate microbeads. *Biomacromolecules* **7,** 1471–1480 (2006).
49. Ricordi, C. *et al.* Islet isolation assessment in man and large animals. *Acta Diabetol. Lat.* **27,** 185–195 (1990).
50. Adewola, A. F. *et al.* Microfluidic perifusion and imaging device for multi-parametric islet function assessment. *Biomed. Microdevices* **12,** 409–417 (2010).
51. Keizer, J. & Magnus, G. ATP-sensitive potassium channel and bursting in the pancreatic beta cell. A theoretical study. *Biophys. J.* **56,** 229–242 (1989).